

# Parallel Simulation of Contact and Actuation for Soft Growing Robots

Yitian Gao<sup>1\*</sup>, Lucas Chen<sup>1\*</sup>, Priyanka Bhovad<sup>2</sup>, Sicheng Wang<sup>2</sup>,  
Zachary Kingston<sup>1</sup>, and Laura H. Blumenschein<sup>2†</sup>

<sup>1</sup> Department of Computer Science, Purdue University

<sup>2</sup> Department of Mechanical Engineering, Purdue University

\* Equal Contribution

† To whom correspondence should be addressed;

E-mail: `lhbblumen@purdue.edu`

September 19, 2025

**Keywords:** Modeling, Control, and Learning for Soft Robots; Soft Growing Robots; GPU-Parallel Simulation

**Abstract:** Soft growing robots, commonly referred to as vine robots, have demonstrated remarkable ability to interact safely and robustly with unstructured and dynamic environments. It is therefore natural to exploit contact with the environment for planning and design optimization tasks. Previous research has focused on planning under contact for passively deforming robots with pre-formed bends. However, adding active steering to these soft growing robots is necessary for successful navigation in more complex environments. To this end, we develop a unified modeling framework that integrates vine robot growth, bending, actuation, and obstacle contact. We extend the beam moment model to include the effects of actuation on kinematics under growth and then use these models to develop a fast parallel simulation framework. We validate our model and simulator with real robot experiments. To showcase the capabilities of our framework, we apply our model in a design optimization task to find designs for vine robots navigating through cluttered environments, identifying designs that minimize the number of required actuators by exploiting environmental contacts. We show the robustness of the designs to environmental and manufacturing uncertainties. Finally, we fabricate an optimized design and successfully deploy it in an obstacle-rich environment.

## 1 Introduction

Soft growing robots, also known as vine robots, are a class of continuum robots that extend from the tip by pressure-driven eversion [26]. Since growth isolates the robot from the environment, vine robots have shown significant beneficial behaviors in tasks with natural pathways to follow, such as medical procedures [19, 5, 2], pipe inspection [39], and archaeology [8]. These behaviors arise from the passive buckling of thin inflated tubes [9, 24], a challenging feature to accurately model.

Multiple works have examined the modeling and use of this passive deformation [20, 17]. However, these works have been limited to purely passive behavior, primarily due to the increased difficulty of modeling the effects of active steering. Other works have also addressed the general simulation of vine robot growth with zero or some pre-formed deformations, including fast, kinematic-only models [18] and dynamic simulations [29, 32]. While slow and accurate FEM simulators [14] have been used to model actuated vine robots [12], these are inefficient for downstream tasks such as planning, control, and design that require high-throughput simulation. Recent work has addressed fast parallel simulation of these robots that accurately captures the bending and buckling behavior intrinsic to vine robots [7]. However, no simulation framework has addressed efficient modeling of actuated vine robots under contact forces.

We present a new modeling framework that captures how vine robots buckle, bend, deform, and extend

while growing into obstacles and steering with series pneumatic artificial muscles (sPAMs) [21]. Our modeling framework independently considers the effects of the actuator and inflated body when calculating the moment balance discretized along the length. Importantly, this leverages a continuous form of the thin-walled inflated tube buckling model that includes partial buckling reactions under small angle deflection [47], allowing us to predict both distributed actuation seen during steering and concentrated actuation seen under environmental contact. We use this model in a parallel simulation framework [7] for fast and accurate prediction of actuated vine robots navigating cluttered environments. We demonstrate that this model is appropriate for long-horizon planning by applying it in a design optimization task: finding vine robot designs that minimize the number of actuators needed to navigate a complex, cluttered environment. Our work provides for the first time the tools to design, model, control, and plan for vine robots while leveraging their full capabilities in both simulated and real environments. We release our simulator as open source: <https://github.com/CoMMLab/ActVineSimPy>.

## 2 Related Work

The flexible, yet inextensible material used in vine robots necessitates the use of novel approaches for *modeling and simulation of vine robot* behavior. While early modeling focused primarily on describing the growth [4], first-principles models for vine robot buckling have been built on inflated thin-shelled beam models [9, 15]. Discrete buckling models, which predict restoring moment independent of bend angle [24, 28], led to kinematic models for contact-induced bending [20], tip localization [16], and obstacle mapping [17]. Recent work has further strengthened this model by considering partial buckling [47].

For distributed surface wrinkling, these constant moment models are not as accurate, so heuristic models have been developed instead, using experimental parameter fitting to create kinematic models [22], or geometrically relating surface strain to resulting general curves [3, 45]. The geometric mappings are generally limited to quasi-static behaviors, though data-driven approaches with Koopman operators have shown that dynamic behaviors can also be empirically modeled [23]. While combined system models have been primarily heuristic, some first-principles actuator models have been developed for series Pneumatic Artificial Muscles (sPAMs) [22] and a range of other common and vine robot-specific actuators [30].

While actuator-beam models describe free-space actuated vine robots, incorporating contact with the environment is challenging. Finite element models built on frameworks like SOFA [14] have been used to successfully model vine robots [32, 12, 44, 49]. However, these approaches are computationally expensive and ill-suited for real-time, at-scale simulation. Other work has simplified the simulations to rigid body models, either using minimal coordinates through virtual joint angles [13] or maximal coordinates with poses of

frames in a global reference with implicit constraints [29]. Previous work has proposed more realistic models for computing strain that respect geometric design parameters [45, 46] and has made these scalable using GPU-accelerated computation frameworks [7]. Overall, our work fills a gap for efficient models that generalize to external and internal forces.

Our *design optimization* approach is built upon sampling-based kinodynamic planning (SBKP) [31, 11, 33], which addresses the general problem of finding a sequence of controls that, when applied to a robot, achieves a goal state. Unlike previous works that use planning to design a vine robot (e.g., [40]), we are given only black-box forward dynamic simulation that captures the vine robot evolution given actuation and environment interactions. Some planners, such as Kinodynamic-RRT\* for linear dynamics [48], arbitrary kinodynamic planning in combination with the AO-X meta algorithm [25] and Stable Sparse RRT (SST) [33], provide asymptotic optimality guarantees, but with no guarantee on when high-quality solutions will be found. Thus, in practice, accelerating the speed of dynamic simulation, the bottleneck of SBKPs, helps them find better solutions faster. Recent work such as Kino-PAX [38] has focused on highly parallel implementations to address these computational challenges. Our approach also leverages the large-scale batch GPU computation of our proposed simulator to improve performance.

### 3 Modeling of Combined Actuation and Growth

Accurately modeling actuated soft growing robots under environmental contact presents a challenge due to the non-linear coupling between actuator force and displacement, beam stiffness or restoring moment, and contact forces. While an actuated robot deployed in free space can be modeled heuristically as one or more constant curvature segments with radius of curvature inversely proportional to actuator pressure [22], and the path of an unactuated vine robot under environmental contact can be robustly predicted based on the visibility graph of the obstacles [18], these heuristic models do not obviously or easily combine. To address this complexity, we develop a unified modeling approach which builds on analytical models of each component separately and then discretizes the vine robot along its length to locally capture the effects of contact and actuation. With this model, the vine robot’s dynamics can be simulated in cluttered environments, where contact interactions significantly influence robot behavior and thus can be exploited for improved navigation performance. In this section, we present each component model separately and then discuss the method to combine the models to accurately predict both actuation and contact with the environment.

### 3.1 Serial Pneumatic Artificial Muscles (sPAMs)

We employ serial Pneumatic Artificial Muscles (sPAMs) to apply distributed actuation along the robot body. A sPAM can be fabricated using a pliable thin-film tube, which has an inflated radius  $R_{act}$ , and constricting that tube to radius  $R_c$  (where  $R_c \ll R_{act}$ ) at regular intervals  $l_0$ , forming a chain of bubbles. When the actuators are completely deflated, they start at full extension (Fig. 1), with constrictions at interval lengths of  $l_0$ . Upon pressurization, the actuator expands radially and, as a result, contracts. The radial expansion continues until the maximum radius at the actuator unit reaches the limit,  $R_{act}$ , saturating the response for that part of the actuator cell. Further pressurization increases this saturated region, further shortening the actuator and decreasing the active region.

To make an actuator component model, we build upon the refined sPAM model in [46], which adapts the ideal PPAM (Pleated Pneumatic Artificial Muscle) model in [10]. The ideal PPAM model does not account for the saturation based on the tube radius, only predicting the cross-section profile which maintains the material length and maximizes volume. The improved sPAM model incorporates actuator saturation by moving the saturated length to shrink the effective length of the actuator when predicting the force-strain output. For a given set of actuator design parameters and pressure inputs:

$$\frac{E(\phi_{Rc}, m) - \frac{1}{2}F(\phi_{Rc}, m)}{\sqrt{m} \cos \phi_{Rc}} = \frac{l_a}{2R_c} \left(1 - \frac{l_0}{l_a} \varepsilon\right), \quad (1a)$$

$$\frac{F(\phi_{Rc}, m)}{\sqrt{m} \cos \phi_{Rc}} = \frac{l_a}{R_c} \left(1 + \frac{a}{2m \cos^2 \phi_{Rc}}\right), \quad (1b)$$

$$a = \frac{P_{act} R_c}{2tE}, \quad \phi_{Rc} = \cos^{-1} \left( \frac{R_c}{R_{act}} \right) \quad (1c)$$

$$F_t = \pi P_{act} R_c^2 \frac{1 - 2m}{2m \cos^2 \phi_{Rc}}. \quad (1d)$$

Here,  $\varepsilon$  denotes the strain,  $F_t$  represents the contraction force.  $m \in (0, 0.5]$  and  $\phi_{Rc} \in (0, \frac{\pi}{2}]$  are dimensionless model parameters, with the former denoting the extent of contraction relative to the full contraction and the latter proportional to the maximum radius of the sPAM unit at a given state.  $l_a$  and  $l_0$  denote the active and total actuator lengths respectively, and  $F(a, b)$  and  $E(a, b)$  are incomplete elliptic integrals of the first and second kind. The pressure-dependent correction factor  $a$  relates the actuator's material properties to force-strain computation. While in the original PPAM model this correlated with material elasticity,  $E$ , and pressure,  $P_{act}$ , with the relatively inextensible tube and constraint materials we instead treat this parameter as an empirically determined constant ( $a = 0.0001$ ). The model accounts for saturation effects by distinguishing between  $l_a$  and  $l_0$  and by setting  $\phi_{Rc}$  based on the saturation and constraint radii (Eq. (1c)). Setting  $l_a = l_0$  and treating  $\phi_{Rc}$  as unknown instead recovers the PPAM model applicable to unsaturated

scenarios. To generate the force-strain output pairs needed for the neural surrogate modeling described in Sec. 4.3, we vary  $m$  over  $m \in (0, 0.5]$ . For each  $m$ , we solve the governing equation for  $\varepsilon$ , and in the unsaturated case, for  $\phi_{Rc}$ . We then compute the contraction force  $F_t$  using these solutions and the prescribed design parameters.

### 3.2 Wrinkling-based Restoring Moment Model

The body of the vine robot is made of a pressurized thin-film tube, which we can treat as an inflated beam. An inflated beam model developed by Comer and Levy [9] demonstrates that the restoring moment of a bent inflated beam increases with surface wrinkling development at bending locations. Previous implementations of this model have focused on the *maximum* restoring moment when the surface is fully wrinkled, especially in works which discuss the buckling of the vine robot under environmental forces [20]. However, for small deflection angles ( $\lesssim 10$  degrees), like those seen in steering, this significantly overestimates the restoring moment. A wrinkling-based model described in [7] captures this angle-to-moment relationship by introducing a critical surface strain  $\varepsilon_{\text{critical}}$  at which wrinkling initiates. The critical strain is obtained by fitting experimentally measured deflection-restoring moment data. The restoring moment  $M$  is computed as:

$$M = \pi P_{\text{vine}} R_{\text{vine}}^3 \frac{\sin(2\gamma_0) + 2\pi - 2\gamma_0}{4(\sin \gamma_0 + (\pi - \gamma_0) \cos \gamma_0)}, \quad (2a)$$

$$\gamma_0 = \cos^{-1} \left( 2 \frac{\varepsilon_{\text{critical}}}{\sin(\theta_{\text{curv}}/2)} - 1 \right). \quad (2b)$$

Here,  $P_{\text{vine}}$  denotes the pressure of the vine robot and  $R_{\text{vine}}$  denotes the radius of the vine robot as shown in Fig. 1.  $\theta_{\text{curv}}$  denotes the turning angle at the point of wrinkling.  $\gamma_0$  represents the angle corresponding to the wrinkled surface of the vine robot as shown in Eq. (2b). Importantly, this model calculates the restoring moment as proportional to the total axial material tension, summed around the tube circumference, i.e.  $\pi P_{\text{vine}} R_{\text{vine}}^2$ . If the vine robot is growing,  $P_{\text{vine}}$  cannot exceed the conditions of quasi-static equilibrium for growth, which are based on the vine robot material and geometry, the internal material tension, and the growth speed [4]. In practice, the effects of growth speed are negligible, so a value for  $P_{\text{vine}}$  can be set by modifying the internal material tension.

### 3.3 Combined Actuation and Contact Model

To combine the component models, we can recognize that the moments exerted by the sPAMs and by the bending of the vine robot segment should balance in free space, and combine to produce a net restoring

moment under dynamic conditions. Without external contact, this equilibrium relationship enables determination of both the strain produced in the vine segment and the radius of curvature in free space. Compared with previous approaches, the wrinkling-based model improves the accuracy of curvature determination, as shown in Fig. 2c.

For developing the forward dynamics simulation that includes contact with the environment, the vine robot is discretized into rigid, serially connected segments of length  $l_{\text{seg}} = 25\text{mm}$ , excluding the last growing segment  $l_{\text{last}}$ , which grows with a predefined growth rate. Thus, the bending behavior of each segment can be considered separately. If the relative bending angle between any two consecutive segments of the vine robot is  $\theta$ , then the actuator strain  $\varepsilon$  corresponding to the bending angle  $\theta$  and net restoring moment  $M_{\text{tot}}(\theta)$  for that segment at each time step is calculated as follows:

$$\varepsilon = \frac{(2R_{\text{vine}} + R_{\text{act}})\theta}{l_{\text{seg}}}, \quad (3a)$$

$$M_{\text{tot}}(\theta) = M(\theta) - F_t(m, \phi_{Rc}, P_{\text{act}}) \cdot (2R_{\text{vine}} + R_{\text{act}}). \quad (3b)$$

Here, the restoring moment of the vine robot segment  $M(\theta)$  is calculated using Eq. (2). The actuator force  $F_t$  and the geometric parameters  $(m, \phi_{Rc})$  for the actuator are calculated using Eq. (1).

## 4 Simulation of Actuation and Growth

Although the individual bending, growth, and contact behaviors are well defined, producing a realistic simulation requires unifying these forces into a single forward function. We combine these forces in a cost-minimization problem, which we use to solve for the next state with a Position-Based Dynamics (PBD) [1] simulation method, which has shown success for rigid and soft body simulations alike [34]. A visual representation of our forward dynamics pipeline is presented in Fig. 3. The pipeline leverages GPU-accelerated batch processing to achieve the throughput requirements necessary for effective design optimization in complex environments.

### 4.1 Position-Based Dynamic Simulation

As described in Sec. 3.3, we chose to discretize the vine into a chain of bodies to produce a finite parameterization. We aim to find the dynamics  $\{\theta\}_{t+1}, l_{\text{last}} = f(\{\theta\}_t, l_{\text{last}})$ .  $l_{\text{last}}$  is the length of the distal segment; all others are held at a fixed length  $l_{\text{seg}}$ .  $\{\theta\}$  is the set of relative bending angles between consecutive bodies in the vine; they describe the local curvature at each point. This rigid body representation was also used in [29, 7], albeit with maximal coordinates. Note that maximal coordinates require extra constraints

to ensure that successive bodies remain connected; our minimal coordinate formulation can only produce connected vines. Here, we formulate the simulation as finding the next state with minimum cost:

$$\text{sim}(\{\theta\}^*) = \arg \min_{\{\theta\}} w_a M_{\text{tot}}(\{\theta\}) + w_b \text{growth}(l_{\text{last}}) + w_c \text{contact}(\{\theta\}, l_{\text{last}}), \quad (4)$$

where “growth” tends to zero as  $l_{\text{last}}$  increases with a predefined growth rate, “contact” measures the amount of penetration of bodies into obstacles, and  $M_{\text{tot}}$  is the restoring moment of the current state as found in Eq. (3). Often, such forces will be in opposition—for example, when the vine is growing into an obstacle, then the growth term will attempt to lengthen  $l_{\text{last}}$  while “contact” will attempt to shorten it. We empirically scaled the weights  $w_a$ ,  $w_b$ , and  $w_c$  to ensure that in all common cases, contacts dominate over moments which in turn dominate growth, thus forbidding segments from growing into the obstacles, with  $w_a = 160$ ,  $w_b = 15$ ,  $w_c = 1$ . Note that we omit velocity and inertial terms as they are insignificant due to the high air resistance and low mass of the vine.

Eq. (4) is highly nonlinear and the relative magnitudes of each force can change rapidly. We use 50 steps of gradient descent to compute  $\text{sim}(\{\theta\}^*)$ , which we found to be sufficient for convergence. Each step of the descent is computed as  $\Delta\{\theta\} = \alpha \frac{\partial \text{sim}(\{\theta\})}{\partial \{\theta\}}$ , with  $\alpha = 0.01$ . We compute gradients using JAX autodifferentiation [6].

## 4.2 Actuator Design Synthesis

Although it is desirable to parameterize actuators along the vine in terms of their turning angle  $\theta_{\text{curv}}$ , actuators are actually parameterized by pressure and length  $P_{\text{act}}$  and  $l_0$ , which are required for simulation and fabrication. Finding these two parameters from  $\theta_{\text{curv}}$  is nontrivial, since multiple solutions of  $P_{\text{act}}$  and  $l_0$  can satisfy any given curvature  $\theta_{\text{curv}}$ . We address this ambiguity by isolating the specific portion of the sPAM model that leads to this non-uniqueness and introducing a cost term to favor an unambiguous single solution out of the space of all possible  $P_{\text{act}}$  and  $l_0$ .

First, we solve for the actuator length  $l_0$  and strain  $\varepsilon$  that satisfy the target curvature  $\theta_{\text{curv}}$  as specified by Eq. (2) and Eq. (1d). Second, we compute the corresponding parameters  $\phi_{Rc}$  and  $m$  by solving the nonlinear system in Eq. (1) using a gradient-based root-finding method; the Levenberg-Marquardt (LM) method [35] proves effective, achieving convergence within  $1 \times 10^{-6}$  tolerance. To avoid local optima inherent in gradient methods, we initialize the LM solver with the lowest-cost candidate from 1000 randomly sampled starting points. Each root-finding iteration requires evaluation of Legendre elliptic integrals of the first and second kind, which lack analytical forms and are approximated to  $1 \times 10^{-10}$  precision using 10 expansions of the Taylor series. This two-stage approach eliminates the one-to-many relationships exhibited in the first

step, ensuring that a single solution is found in both stages of the actuator synthesis process.

To resolve ambiguities, we impose a cost function that favors higher pressure  $P_{\text{act}}$  over larger actuator length  $l_0$ , except where such preferences would yield infeasible solutions. When multiple valid combinations of  $P_{\text{act}}$  and  $l_0$  exist, we select the design with the highest pressure from the feasible set. This selection criterion is motivated by experimental observations that higher pressures produce more consistent curvatures despite fabrication tolerances and modeling uncertainties. Although the parameter sets  $\{l_0\}$  and  $\{P_{\text{act}}\}$  form continuous one-dimensional manifolds in the design space, we restrict sampling to discrete values due to physical fabrication constraints. Specifically, our fabrication process is limited by a 1mm accuracy for  $l_0$  and we are only capable of providing pressures from a discrete set, which limits the available parameter values. This process ultimately yields optimal pressure  $P_{\text{act}}^*$  and corresponding actuator length  $l_0^*$ . We also note that throughout this work, we maintain constant values for several parameters that were excluded from the notation: constriction radius  $R_c = 5\text{mm}$ , actuator tube radius  $R_{\text{act}} = 17.18\text{mm}$ , vine segment radius  $R_{\text{vine}} = 33.35\text{mm}$ , and vine robot growth pressure  $P_{\text{vine}} = 1.5\text{psi}$ .

### 4.3 Neural Surrogate

As detailed in Sec. 4.2, actuator design parameter generation requires precise solutions to the sPAM model in Eq. (1). While numerical methods provide reasonable performance for individual solutions (requiring only milliseconds), we wish to use our actuator model in a design optimization task, which demands hundreds of thousands of simulation steps, corresponding to millions of individual sPAM evaluations. In this high-throughput regime, numerical methods become computationally prohibitive. We instead approximate the sPAM model using a neural network surrogate. Analysis of the function reveals smooth and monotonic behavior of the output with respect to input parameters. The absence of high-frequency features and the single-mode nature of the function make accurate approximation by a neural surrogate possible, as such networks excel at fitting smooth, well-behaved data. Furthermore, neural networks can be evaluated efficiently in parallel.

Through hyperparameter optimization, we determined that a  $2 \times 32 \times 2$  multi-layer perceptron with ReLU nonlinearities [36] and He initialization [27] provided the best balance of speed and accuracy. We trained the surrogate on 40,000 ground truth samples. Performance evaluation results are presented in Fig. 4. The surrogate achieves four orders of magnitude improvement in throughput (at experimental batch sizes) while maintaining average MSE loss of 0.003 (with outputs normalized). These computational speeds enable simulation faster than real-time, making our design optimization tractable for complex environments.

## 5 Long Horizon Design Optimization

In contact-rich environment navigation problems, contacts, nonlinear bending mechanics, and growth dynamics jointly determine vine behavior. Analytical or inverse numerical solutions for vine design under these coupled effects are either intractable or computationally challenging, necessitating approaches that use forward simulation. We formulate the design optimization problem for soft growing robots as a sampling-based kinodynamic planning (SBKP) problem [31]. SBKPs provide a framework for solving problems that can only be explored with forward dynamic simulation—in our problem, we simulate the vine robot under varying actuator design parameters and propagate the vine robot forward in time by simulating constant growth with sampled actuator designs.

Specifically, we use Stable Sparse RRT\* (SST\*) [33], which provides asymptotic near-optimality guarantees. That is, as the number of samples drawn goes to infinity, the cost of the solution converges to  $1 + \epsilon$  times the optimal solution. This approach enables the discovery of robot designs that exploit environmental contact to achieve navigation goals while minimizing actuator requirements.

We use the simulation framework from Sec. 4 to provide batch simulation capabilities for the planner. At each iteration, the planner chooses a varying time of execution and actuation parameters to propagate, sampling from existing nodes in the search tree to grow from—the nodes in the search tree are parameterized by the pose of the tip of the vine in space. An example of how the planner progresses its search with these batch rollouts is shown in Fig. 7.

### 5.1 Reverse Tree Heuristic

To reduce SST\*'s computational cost, we incorporate a reverse tree search heuristic that uses geometric (not dynamic) rollouts of designs to guide exploration toward goal-reaching areas. Cost-to-go heuristics improve search efficiency in methods like AIT\* [42] and GBRRT [37], which employ bidirectional trees where the reverse tree provides guidance rather than direct connection. Our reverse tree uses RRT\* [41] in OMPL [43] with biarc interpolation, providing asymptotic optimality. Biarcs are two tangentially continuous circular arcs and align well with the piecewise constant curvature behavior of actuated vine segments. We modify SST\*'s cost function to include both cost-to-come and estimated cost-to-go from the reverse geometric tree, which establishes upper bounds on path costs used by the kinodynamic planner. The objective function minimizes the number of curved segments (actuator count) with path length as a tie-breaker. For state validity checking, we verify that the curvature of sampled biarcs  $\theta_{\text{curv}}$  lies within numerically determined feasible minimum and maximum values rather than computing explicit actuator designs, maintaining planning soundness while reducing computation.

## 6 Experimental Results

We evaluate our modeling and simulation framework with real-world validation of the simulator against physical vine robot behavior and assessment of the design optimization framework across a number of challenging environments.

### 6.1 Physical Validation

For initial validation, we constructed a single-obstacle environment to evaluate the accuracy of our contact and actuation models under well-defined conditions. We prepared three distinct contact interaction configurations: (1) an acute angle of contact, designed to bend into the contact normal (increasing curvature under contact), (2) an obtuse angle of contact, designed to bend away from the contact normal (decreasing curvature under contact), and (3) a head-on contact, which leads to buckling behavior as the beam bends away from the contact normal (Fig. 5). Due to the nonlinearity of the sPAM bending model and contact mechanics, these configurations exhibit asymmetric behaviors and yield substantially different final robot configurations. These experiments demonstrate that our simulator captures the fundamental contact-actuation coupling accurately when the initial contact conditions match between simulation and reality. However, small deviations in the simulator prior to obstacle contact can cause divergences on contact, as contact forces often dominate and can “funnel” the robot into different homotopy classes of motion through the environment (e.g., hitting on one side or the other). This sensitivity is underscored by our robustness evaluation in Sec. 6.4.

### 6.2 Long-Horizon Design Optimization

We assess the effectiveness of our design optimization framework across six different environments, each designed to test specific aspects of the planning approach and environmental interaction capabilities. The evaluation environments, illustrated in Fig. 6, span a range of planning challenges:

1. **Plus:** A uniform grid of plus-shaped obstacles creating multiple viable paths, testing the planner’s ability to identify better solutions among alternatives.
2. **Maze:** A structured environment with few solutions and many dead-ends, evaluating planning robustness in constrained solution spaces.
3. **Pickone:** Multiple identical passages with only one leading to the goal, evaluating the effectiveness of heuristic guidance.

4. **Needle**: A series of narrow passages requiring precision to navigate, evaluating the planner’s ability to handle tight geometric constraints.
5. **Long**: An environment with strategically positioned contacts that must be exploited to avoid dead-end passages, testing contact-based navigation.
6. **Tube**: A minimal environment to test whether the planner can identify trivial solutions.

Our design optimization framework successfully identified feasible solutions for all evaluation environments, as demonstrated in Fig. 6. Even in the more difficult environments such as **Maze**, **Long**, and **Needle**, which are cluttered, full of dead ends, and require precise movement, our planner effectively discovered minimum-actuator designs that exploited contact with the environment to achieve the task objective.

We evaluated the planner with and without the reverse tree heuristic over 30 independent runs on each environment; statistics are reported in Tab. 1. The planner had consistent performance; all environments achieved initial solutions within 60 seconds on an AMD Ryzen 9 5900 CPU and NVIDIA RTX 3050 GPU, enabling interactive design iteration and deployment with a desktop computer.

The **Long** environment validates the core hypothesis of our approach: the planner successfully identified designs that exploit deliberate contact interactions to navigate passages that would be inaccessible without environmental support. This demonstrates the practical advantage of contact-aware design optimization over traditional collision-avoidance approaches. This is also evidenced in the **Tube** environment, where the planner consistently produced near-optimal solutions with only one or two segments, indicating successful identification of minimal-actuation designs despite the availability of more complex alternatives. For environments with multiple viable solution paths (e.g., **Plus** and **Maze**), the planner demonstrated breadth of exploration, identifying diverse design alternatives that utilize different environmental corridors. This capability provides designers with multiple implementation options with different potential robustness against environmental variations.

Surprisingly, the reverse tree heuristic did not provide substantial performance improvements across the evaluated environments, even for more complex scenarios like **Pickone** and **Maze** that feature dead-ends and branching passages where heuristic guidance would be expected to provide benefit. We hypothesize that the natural funnel-like behavior exhibited by vine robot dynamics—particularly the tendency for contact interactions to guide the robot toward feasible solutions—reduces the need for explicit guidance in environments of the scale we evaluated. This observation suggests that the inherent physics of vine robots implicitly guides the system, obviating the need for other heuristics.

### 6.3 Design Optimization in Reality

To evaluate our design optimization approach, we constructed a multi-obstacle environment with many potential solutions that required exploitation of contacts for successful navigation. First, we applied our design optimization framework to find a vine robot actuator design that would navigate the robot from a specified start pose to a target goal region. Second, we fabricated the generated designs. Third, we deployed these physical robots and compared their behavior against the simulator’s predictions. The results shown in Fig. 8 demonstrate that our simulator accurately models both contact mechanics and bending behavior and that our generated designs translate effectively to physical implementations. Quantitative analysis of the difference between simulated and real markers on the robot shows mean deviations (using Euclidean distance) of 26–43mm (note that  $R_{\text{vine}} = 33.35\text{mm}$ ). Deviations of this magnitude are within acceptable tolerance for the navigation tasks considered, particularly given the inherent uncertainties in fabrication, deployment, and measurement. This is further affirmed by our robustness tests (Sec. 6.4), where minor deviations in vine bending control have little effect on overall vine trajectory due to effects from contact forces.

### 6.4 Robustness of Designs

Fig. 9 presents the success rate of reaching the goal region as a function of uncertainty in both the environment and actuation parameters, in the same environment as Fig. 8. We model environmental uncertainty through Gaussian perturbations of obstacle positions and sizes with gradually increasing variance levels. Similarly, actuation uncertainty is modeled through perturbations of actuator pressure and length parameters. For each level of uncertainty, we evaluate success rates across 1000 trials.

Results show graceful degradation of task satisfaction with increasing uncertainty levels, and that designs generated by our framework have inherent tolerance to uncertainties, particularly when contact interactions provide environmental guidance that compensates for actuation variations. This supports the deployment of found designs in real-world environments where perfect transfer of simulation to reality is unattainable. This evaluation also reinforces our earlier observation that contact-guided navigation provides natural error correction that maintains overall success despite small deviations in behavior. An interesting direction for future work is to explicitly target designs that exploit behaviors that are inherently more robust to uncertainty due to this effect.

## 7 Discussion

This work presents a unified modeling framework for soft growing robots that accurately captures the coupled effects of pneumatic actuation, beam mechanics, and environmental contact. We also present a means of efficiently simulating vine robots using this model with a neural surrogate approach that achieves four orders of magnitude computational speedup for sPAM model evaluation while maintaining accuracy, enabling faster-than-real-time simulation. We use this fast simulation framework to develop a contact-aware design optimization framework built upon asymptotically near-optimal sampling-based kinodynamic planning to find designs of vine robots with minimal numbers of actuators. The design optimization framework successfully found solutions that leverage contact to navigate through otherwise inaccessible passages, demonstrating how soft growing robots can exploit environmental contact for robust behavior even under design and environmental uncertainty. The model and simulator were validated through real robot experiments.

While our model and design framework show promising results, several limitations remain. The current model is restricted to planar environments and makes several assumptions regarding pressure dynamics. Moreover, our design framework was tested in scenarios that were too simple to demonstrate the effectiveness of long-horizon guidance through the geometric heuristic, due to manufacturing limits. Future work should investigate more complex tasks that require high-level reasoning, such as manipulation and long-horizon navigation. While we did not show results for other cost functions, our design optimization framework supports any function of the robot’s shape. We plan to investigate costs that leverage the funneling effect of contact forces to enhance robustness rather than increasing uncertainty.

## Acknowledgments

We would like to thank Gilbert Chang for feedback on this manuscript.

## Authorship Contribution Statement

YG and LC developed and evaluated the simulation and planning framework and assisted in physical validation. PB and SW developed the combined actuation and contact moment model and physically validated the approach. ZK and LHB supervised the project. All authors discussed the results and contributed to the final manuscript.

## Conflict of Interest Statement

The authors have no conflicts of interest to declare.

## Funding Statement

This work was supported in part by NSF FRR 2308653. This material is based upon work supported by the United States Air Force (AFMC AFRL/RXNW) under Air Force Contract No. FA2394-24-C-B060.

## References

- [1] Jan Bender, Matthias Müller, Miguel A Otaduy, Matthias Teschner, and Miles Macklin. A survey on position-based simulation methods in computer graphics. *Computer Graphics Forum*, 33(6):228–251, 2014.
- [2] Pierre Berthet-Rayne, SM Hadi Sadati, Georgios Petrou, Neel Patel, Stamatia Giannarou, Daniel Richard Leff, and Christos Bergeles. Mammobot: A miniature steerable soft growing robot for early breast cancer detection. *IEEE Robotics and Automation Letters*, 6(3):5056–5063, 2021.
- [3] Laura H. Blumenschein, Margaret Koehler, Nathan S. Usevitch, Elliot Wright Hawkes, D. Caleb Rucker, and Allison M. Okamura. Geometric solutions for general actuator routing on inflated-beam soft growing robots. *IEEE Transactions on Robotics*, 38(3):1820–1840, 2022.
- [4] Laura H Blumenschein, Allison M Okamura, and Elliot W Hawkes. Modeling of bioinspired apical extension in a soft robot. In *Conference on Biomimetic and Biohybrid Systems*, pages 522–531, 2017.
- [5] Korn Borvorntanajanya, Shen Treratanakulchai, Ferdinando Rodriguez y Baena, and Enrico Franco. Model-based tracking control of a soft growing robot for colonoscopy. *IEEE Transactions on Medical Robotics and Bionics*, 2024.
- [6] James Bradbury, Roy Frostig, Peter Hawkins, Matthew James Johnson, Chris Leary, Dougal Maclaurin, George Necula, Adam Paszke, Jake VanderPlas, Skye Wanderman-Milne, and Qiao Zhang. JAX: composable transformations of Python+NumPy programs, 2018.
- [7] Lucas Chen, Yitian Gao, Sicheng Wang, Francesco Fuentes, Laura H. Blumenschein, and Zachary Kingston. Physics-grounded differentiable simulation for soft growing robots. In *IEEE International Conference on Soft Robotics*, pages 1–8, 2025.

- [8] Margaret M Coad, Laura H Blumenschein, Sadie Cutler, Javier A Reyna Zepeda, Nicholas D Naclerio, Haitham El-Hussieny, Usman Mehmood, Jee-Hwan Ryu, Elliot W Hawkes, and Allison M Okamura. Vine robots. *IEEE Robotics and Automation Magazine*, 27(3):120–132, 2019.
- [9] R. L. Comer and Samuel Levy. Deflections of an inflated circular-cylindrical cantilever beam. *AIAA Journal*, 1(7):1652–1655, 1963.
- [10] Frank Daerden. *Conception and realization of pleated pneumatic artificial muscles and their use as compliant actuation elements*. Ph.D. thesis, Vrije Universiteit Brussel, 1999.
- [11] Bruce Donald, Patrick Xavier, John Canny, and John Reif. Kinodynamic motion planning. *Journal of the ACM*, 40(5):1048–1066, November 1993.
- [12] Cosima du Pasquier, Sehui Jeong, and Allison M Okamura. Finite element modeling of pneumatic bending actuators for inflated-beam robots. *IEEE Robotics and Automation Letters*, 2023.
- [13] Haitham El-Hussieny, Usman Mehmood, Zain Mehdi, Sang-Goo Jeong, Muhammad Usman, Elliot W Hawkes, Allison M Okamura, and Jee-Hwan Ryu. Development and evaluation of an intuitive flexible interface for teleoperating soft growing robots. In *IEEE/RSJ International Conference on Intelligent Robots and Systems*, pages 4995–5002, 2018.
- [14] François Faure, Christian Duriez, Hervé Delingette, Jérémie Allard, Benjamin Gilles, Stéphanie Marchesseau, Hugo Talbot, Hadrien Courtecuisse, Guillaume Bousquet, Igor Peterlik, et al. SOFA: A multi-model framework for interactive physical simulation. *Soft Tissue Biomechanical Modeling for Computer Assisted Surgery*, pages 283–321, 2012.
- [15] WB Fichter. *A theory for inflated thin-wall cylindrical beams*, volume D-3466. National Aeronautics and Space Administration, 1966.
- [16] Eugenio Frias-Miranda, Alankriti Srivastava, Sicheng Wang, and Laura H. Blumenschein. Vine robot localization via collision. In *IEEE/RSJ International Conference on Intelligent Robots and Systems*, pages 2515–2521, 2023.
- [17] Francesco Fuentes and Laura H. Blumenschein. Mapping unknown environments through passive deformation of soft, growing robots. In *IEEE/RSJ International Conference on Intelligent Robots and Systems*, pages 2522–2527, 2023.
- [18] Francesco Fuentes, Serigne Diagne, Zachary Kingston, and Laura H. Blumenschein. Exteroception through proprioception: Sensing through improved contact modeling for soft growing robots. *International Journal of Robotics Research*, 2025. Under Review.

- [19] Cédric Girerd, Anna Alvarez, Elliot W Hawkes, and Tania K Morimoto. Material scrunching enables working channels in miniaturized vine-inspired robots. *IEEE Transactions on Robotics*, 2024.
- [20] Joseph D Greer, Laura H Blumenschein, Ron Alterovitz, Elliot W Hawkes, and Allison M Okamura. Robust navigation of a soft growing robot by exploiting contact with the environment. *The International Journal of Robotics Research*, 39(14):1724–1738, 2020.
- [21] Joseph D Greer, Tania K Morimoto, Allison M Okamura, and Elliot W Hawkes. Series pneumatic artificial muscles (spams) and application to a soft continuum robot. In *IEEE International Conference on Robotics and Automation*, pages 5503–5510, 2017.
- [22] Joseph D. Greer, Tania K. Morimoto, Allison M. Okamura, and Elliot W. Hawkes. A soft, steerable continuum robot that grows via tip extension. *Soft Robotics*, 6(1):95–108, 2019.
- [23] David A Haggerty, Michael J Banks, Ervin Kamenar, Alan B Cao, Patrick C Curtis, Igor Mezić, and Elliot W Hawkes. Control of soft robots with inertial dynamics. *Science Robotics*, 8(81):eadd6864, 2023.
- [24] David A. Haggerty, Nicholas D. Naclerio, and Elliot W. Hawkes. Characterizing environmental interactions for soft growing robots. In *IEEE/RSJ International Conference on Intelligent Robots and Systems*, pages 3335–3342, 2019.
- [25] Kris Hauser and Yilun Zhou. Asymptotically optimal planning by feasible kinodynamic planning in a state–cost space. *IEEE Transactions on Robotics*, 32(6):1431–1443, 2016.
- [26] Elliot W Hawkes, Laura H Blumenschein, Joseph D Greer, and Allison M Okamura. A soft robot that navigates its environment through growth. *Science Robotics*, 2(8), 2017.
- [27] Kaiming He, Xiangyu Zhang, Shaoqing Ren, and Jian Sun. Delving deep into rectifiers: Surpassing human-level performance on imagenet classification. In *IEEE International Conference on Computer Vision*, pages 1026–1034, 2015.
- [28] Joel Hwee, Andrew Lewis, Allison Raines, and Blake Hannaford. Kinematic modeling of a soft evertng robot from inflated beam theory. In *IEEE International Conference on Soft Robotics*, pages 1–6, 2023.
- [29] Rianna Jitosho, Nathaniel Agharese, Allison Okamura, and Zac Manchester. A dynamics simulator for soft growing robots. In *IEEE International Conference on Robotics and Automation*, pages 11775–11781, 2021.

- [30] Alexander M. Kübler, Cosima du Pasquier, Andrew Low, Betim Djambazi, Nicolas Aymon, Julian Förster, Nathaniel Agharese, Roland Siegwart, and Allison M. Okamura. A comparison of pneumatic actuators for soft growing vine robots. *Soft Robotics*, 11(5):857–868, 2024.
- [31] S.M. LaValle. *Planning Algorithms*. Cambridge University Press, 2006.
- [32] Pengchun Li, Yongchang Zhang, Guangyu Zhang, Dekai Zhou, and Longqiu Li. A bioinspired soft robot combining the growth adaptability of vine plants with a coordinated control system. *Research*, 2021.
- [33] Yanbo Li, Zakary Littlefield, and Kostas E. Bekris. Asymptotically optimal sampling-based kinodynamic planning. *The International Journal of Robotics Research*, 35(5):528–564, 2016.
- [34] Miles Macklin, Matthias Müller, and Nuttapong Chentanez. XPBD: Position-based simulation of compliant constrained dynamics. In *International Conference on Motion in Games*, page 49–54, 10 2016.
- [35] Jorge J. Moré. The Levenberg-Marquardt algorithm: Implementation and theory. In G. A. Watson, editor, *Numerical Analysis*, pages 105–116, Berlin, Heidelberg, 1978. Springer Berlin Heidelberg.
- [36] Vinod Nair and Geoffrey E Hinton. Rectified linear units improve restricted boltzmann machines. In *International Conference on Machine Learning*, pages 807–814, 2010.
- [37] Sharan Nayak and Michael W. Otte. Bidirectional sampling based search without two point boundary value solution. *CoRR*, abs/2010.14692, 2020.
- [38] Nicolas Perrault, Qi Heng Ho, and Morteza Lahijanian. Kino-PAX: Highly parallel kinodynamic sampling-based planner. *IEEE Robotics and Automation Letters*, 10(3):2430–2437, 2025.
- [39] Yimeng Qin, Allison M Okamura, and Marco Salathe. Design, control, and modeling for soft growing robot deployment for nuclear material inspection. In *Institute of Nuclear Materials Management Annual Meeting*, 2024.
- [40] M. Selvaggio, L. A. Ramirez, N. D. Naclerio, B. Siciliano, and E. W. Hawkes. An obstacle-interaction planning method for navigation of actuated vine robots. In *IEEE International Conference on Robotics and Automation*, pages 3227–3233, 2020.
- [41] Kiril Solovey, Lucas Janson, Edward Schmerling, Emilio Frazzoli, and Marco Pavone. Revisiting the asymptotic optimality of RRT. In *IEEE International Conference on Robotics and Automation*, pages 2189–2195, 2020.

- [42] Marlin P. Strub and Jonathan D. Gammell. Adaptively informed trees (AIT $^*$ ): Fast asymptotically optimal path planning through adaptive heuristics. In *IEEE International Conference on Robotics and Automation*, 2020.
- [43] Ioan A. Sucan, Mark Moll, and Lydia E. Kavraki. The Open Motion Planning Library. *IEEE Robotics and Automation Magazine*, 19(4):72–82, December 2012. <https://ompl.kavrakilab.org>.
- [44] Panagiotis Vartholomeos, Zicong Wu, SM Hadi Sadati, and Christos Bergeles. Lumped parameter dynamic model of an eversion growing robot: Analysis, simulation and experimental validation. In *IEEE International Conference on Robotics and Automation*, pages 12734–12740, 2024.
- [45] Sicheng Wang and Laura H. Blumenschein. A geometric design approach for continuum robots by piecewise approximation of freeform shapes. In *IEEE/RSJ International Conference on Intelligent Robots and Systems*, pages 5416–5423, 2022.
- [46] Sicheng Wang and Laura H. Blumenschein. Refined modeling for serial pneumatic artificial muscles enables model-based actuation design. In *IEEE International Conference on Soft Robotics*, pages 800–807, 2024.
- [47] Sicheng Wang, Eugenio Frias-Miranda, Antonio Alvarez Valdivia, and Laura H Blumenschein. Anisotropic stiffness and programmable actuation for soft robots enabled by an inflated rotational joint. *arXiv Preprint arXiv:2410.13003*, 2024.
- [48] Dustin J. Webb and Jur van den Berg. Kinodynamic RRT $^*$ : Asymptotically optimal motion planning for robots with linear dynamics. In *IEEE International Conference on Robotics and Automation*, pages 5054–5061, 2013.
- [49] Zicong Wu, Mikel De Iturrate Reyzabal, SM Hadi Sadati, Hongbin Liu, Sebastien Ourselin, Daniel Leff, Robert K Katzschnmann, Kawal Rhode, and Christos Bergeles. Towards a physics-based model for steerable eversion growing robots. *IEEE Robotics and Automation Letters*, 8(2):1005–1012, 2023.

## Supplementary Information

The vine robot main body and sPAMs are fabricated with LDPE (low-density polyethylene) tubes of  $50\mu\text{m}$  thickness. The inflated radius of the vine robot main body  $R_{\text{vine}} = 33.35\text{mm}$  and the actuator tube radius  $R_{\text{act}} = 17.18\text{mm}$ . We use 3-D printed brackets to constrict the actuator tube to radius  $R_c$  at regular intervals  $l_0$ , forming a chain of sPAMs. The 3-D printed bracket has a slot through which the actuators were attached to the vine robot tube using double-sided tape adhesive (True Tape LLC., CO, USA). This method of attachment for sPAMs ensures the actuators do not delaminate from the vine robot tube when pressurized. We control the vine robot growth and steering pressure with feedback-controlled pressure regulators (QB3, Proportion Air, IN, USA). An Arduino UNO R4 Minima and a custom QB3 shield are used to send pressure commands. For motion tracking, green circular markers are attached to the spine of the vine robot and tracked via an overhead camera. The individual frames from the collected videos are segmented in Python using image processing tools from OpenCV2.

## Figures and Tables

Env	Default			No Geo		
	Solve time	Best cost	Iter time	Solve time	Best cost	Iter time
<b>Plus</b>	20.63s	4.24	5.65s	19.50s	4.04	5.71s
<b>Maze</b>	19.95s	3.82	6.86s	23.64s	3.91	6.49s
<b>Pickone</b>	15.94s	3.08	6.06s	14.66s	3.16	5.88s
<b>Needle</b>	46.08s	5.09	4.97s	50.50s	5.38	5.00s
<b>Long</b>	27.95s	5.07	6.07s	27.88s	5.21	5.44s
<b>Tube</b>	6.25s	1.24	5.88s	5.73s	1.24	5.82s

Table 1: Comparison of planning performance with (Default) and without (No Geo) geometric heuristic guidance. **Solve time:** average time to first solution. **Best cost:** average final cost after optimization. **Iter time:** average time per iteration of SST\*. Surprisingly, the geometric heuristic provides minimal performance improvement across evaluated environments. We hypothesize that contact forces the vine robot into “funnels,” guiding it along corridors in the environment.

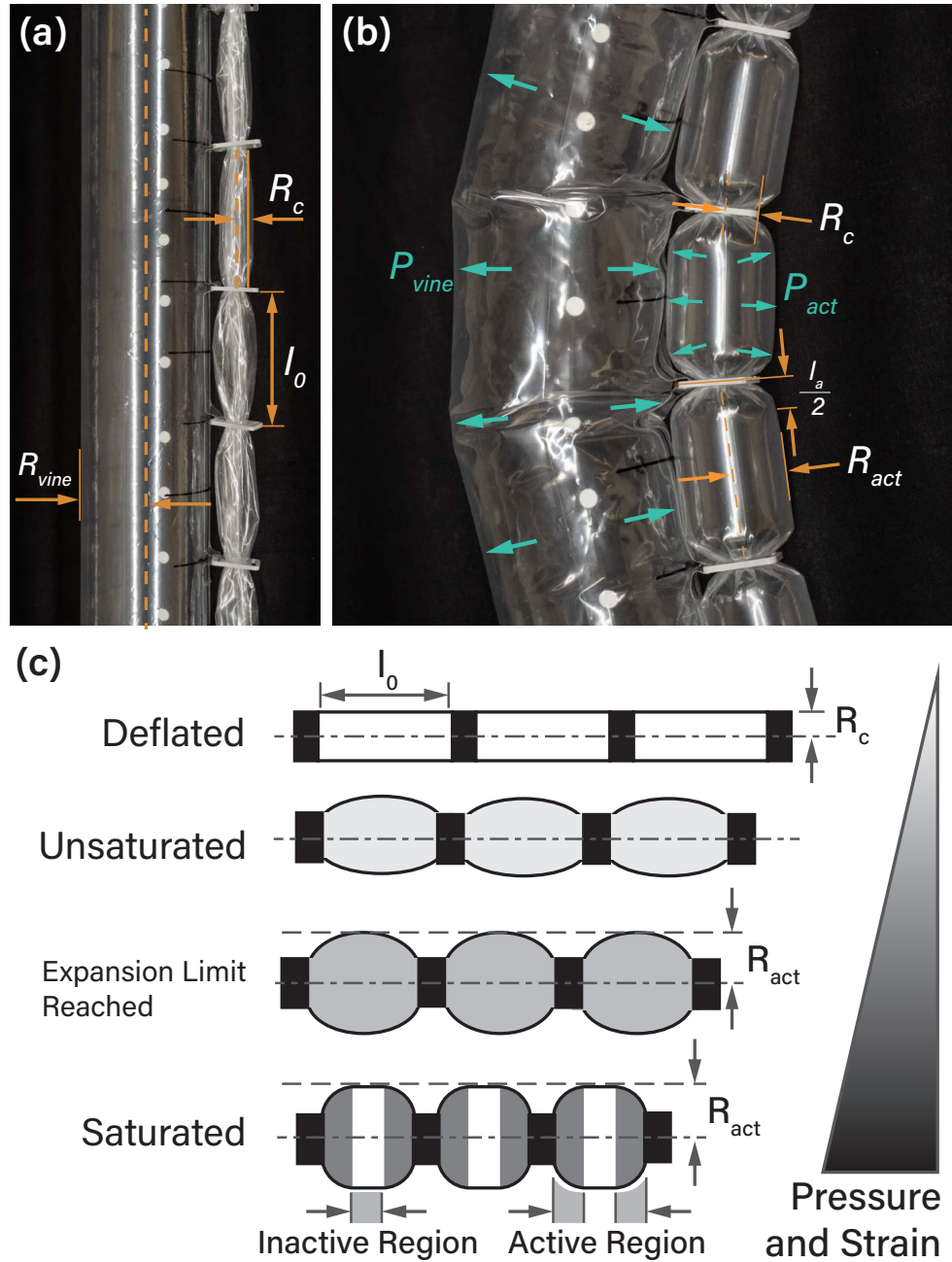


Figure 1: (a), (b): Variable definitions for the sPAM and inflated beam model. (c): Illustration of sPAM states from completely deflated with zero strain (top) to saturated with maximal strain (bottom). Darker color indicates higher input pressure and greater contraction.

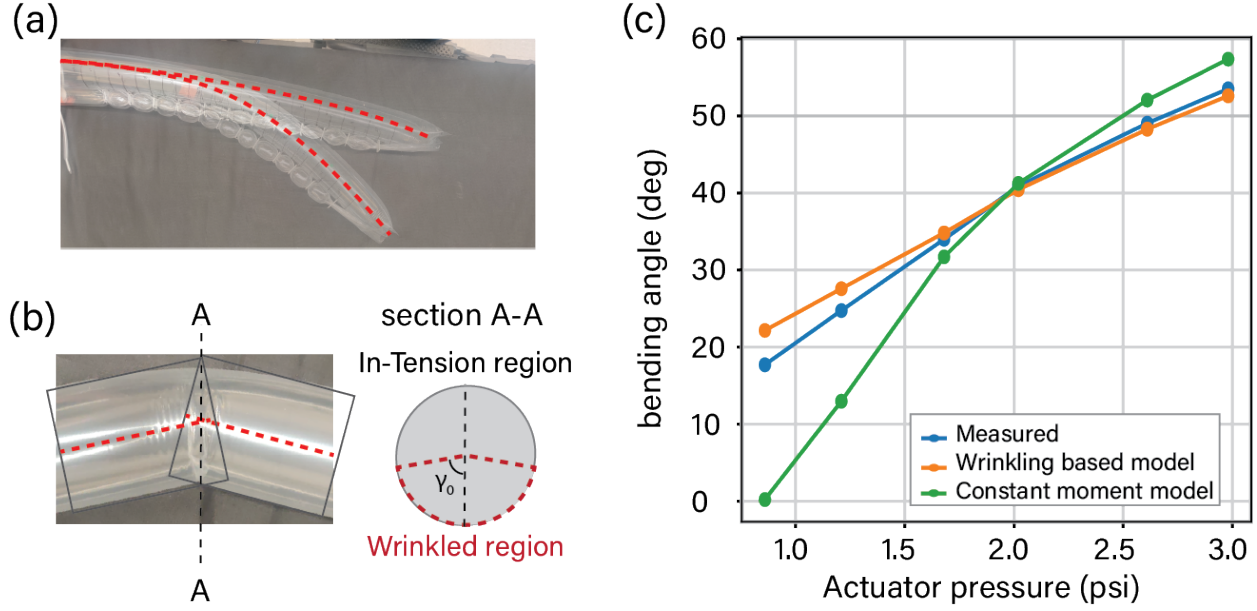
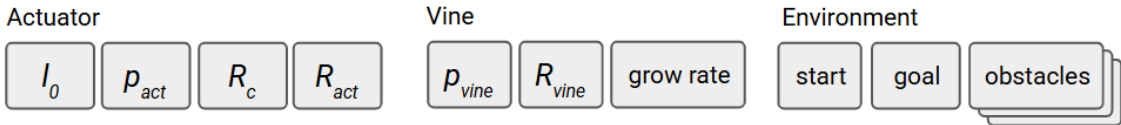


Figure 2: (a): Vine segment bending under sPAM actuation. (b): Vine segment wrinkled and tensioned regions depicting  $\gamma_0$ . (c): Comparison of measured bending angles with theoretical estimations using wrinkling based model and constant moment model.

### Parameterization



### Forward Simulation

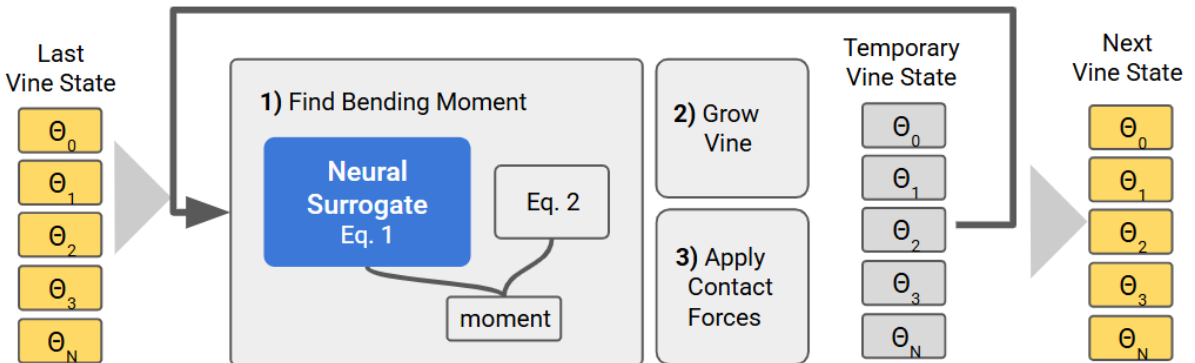


Figure 3: Forward dynamics model for the position of the vine. The whole function runs batched on the GPU. We discretize the vine and actuator into individual joints used internally in the simulation; this is distinct from the actual length of the fabricated actuator. We leverage a neural surrogate to rapidly generate predictions of the sPAM model.

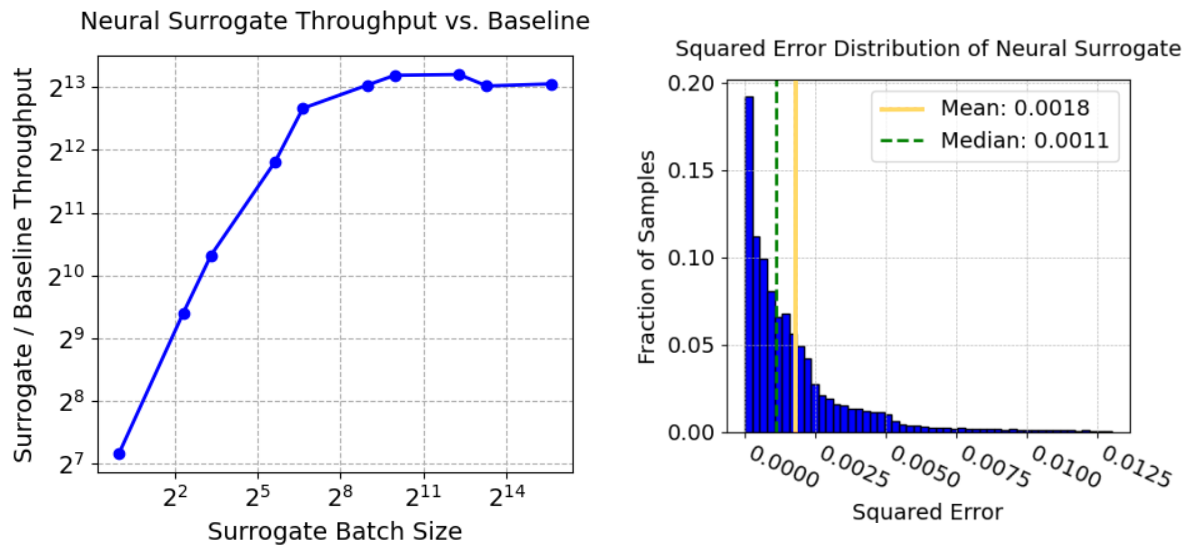


Figure 4: **Left:** The neural surrogate demonstrates a major speed up over the baseline unbatched method, especially as the batch size increases. Batched GPU processing can greatly accelerate parallelizable simulation tasks. **Right:** Distribution of neural surrogate squared error as compared with ground truth numeric method. We uniformly sampled 40,000 values over the surrogate's input space and normalized the outputs.

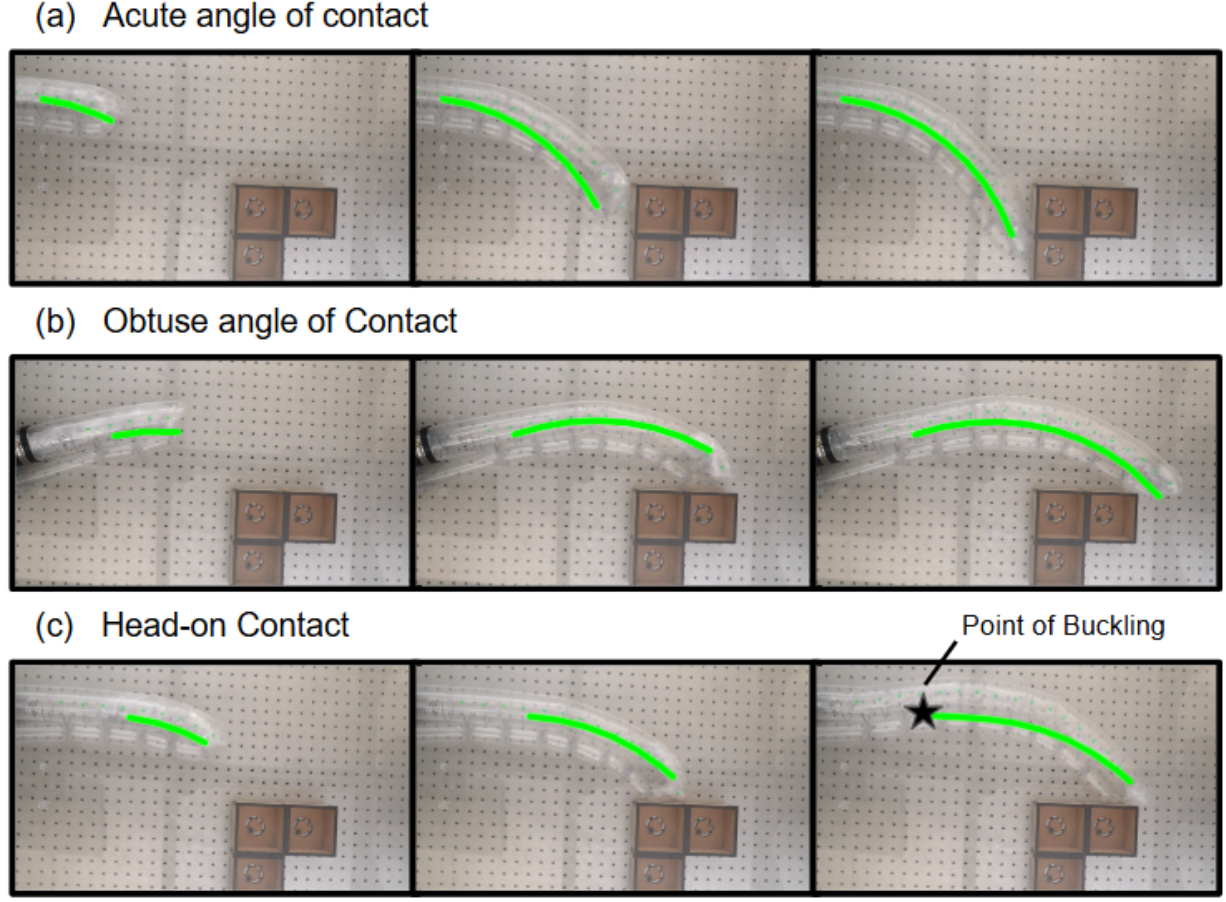


Figure 5: Single-obstacle environment experiment comparing simulated predictions for different obstacle contact conditions. (a) Acute angle of contact, (b) Obtuse angle of contact, (c) Head-on contact. The robot buckles at a point near its base.

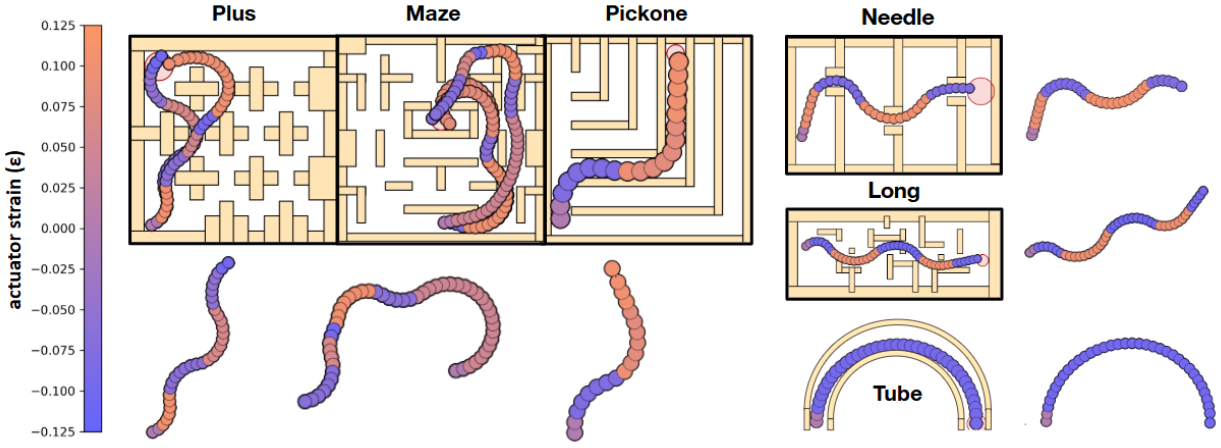


Figure 6: Multiple solutions found for the six evaluation environments by our design optimization approach. Our approach successfully identified solutions for: complex navigation through clutter (**Plus**, **Maze**, and **Pickone**), navigation through tight constraints (**Needle**), precise contact exploitation (**Long**), and trivial solutions when they exist (**Tube**). Free-floating images display the final actuated vine shape in free space.

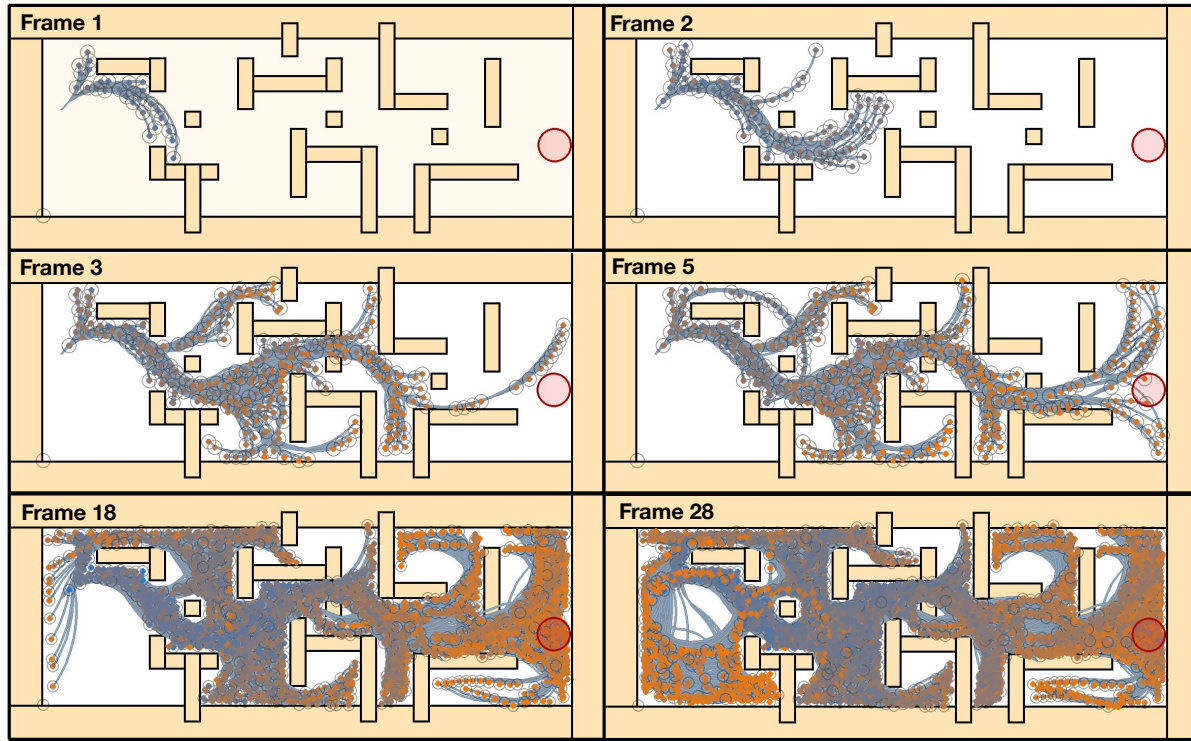


Figure 7: Progression of planning in the **Long** environment, illustrating rapid initial exploration followed by convergent optimization. The planner identifies an initial solution by iteration 5, then refines the design through exploration of alternative contact-exploitation strategies.

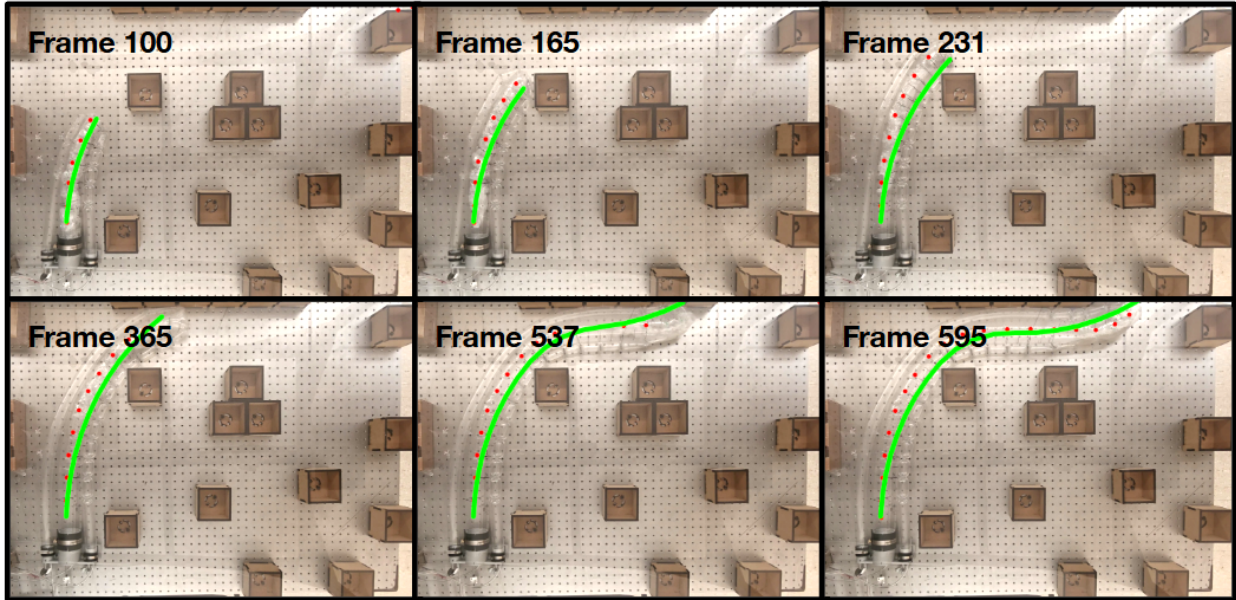


Figure 8: Physical validation experiment comparing simulated predictions (green) with real vine robot behavior in a complex multi-obstacle environment. The designed actuator configuration successfully navigates the cluttered environment in both simulation and reality, with mean position errors of 26–43mm.

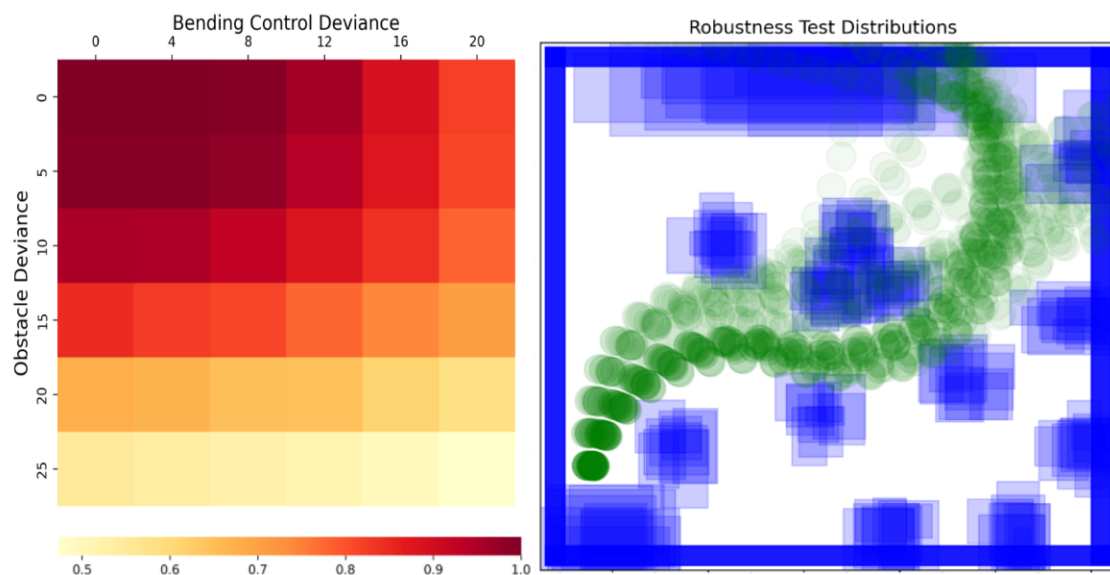


Figure 9: **Left:** Robustness test success rates. Scale for obstacle shift is percent size difference and position change in millimeters. Scale for bending control shift is percent change to actuator pressure and actuator length. Each division was run with a sample size of 1000. **Right:** 10 sampled environments at highest deviation and 60 designs rolled out. The "funneling" effects of contacts are clear: even with variations in obstacles and designs, the vine robot is pushed down similar trajectories.